optica

Photonic chip for laser stabilization to an atomic vapor with 10⁻¹¹ instability

Matthew T. Hummon,[1,*] ⓘ Songbai Kang,[1,2] Douglas G. Bopp,[1,2] Qing Li,[3] Daron A. Westly,[3] Sangsik Kim,[4] Connor Fredrick,[1,2] Scott A. Diddams,[1] Kartik Srinivasan,[3] Vladimir Aksyuk,[3] ⓘ and John E. Kitching[1]

[1]Time and Frequency Division, National Institute of Standards and Technology (NIST), Boulder, Colorado 80305, USA
[2]Department of Physics, University of Colorado, Boulder, Colorado 80309, USA
[3]Center for Nanoscale Science and Technology, National Institute of Standards and Technology, Gaithersburg, Maryland 20899, USA
[4]Department of Electrical and Computer Engineering, Texas Tech University, Lubbock, Texas 79409, USA
*Corresponding author: matthew.hummon@nist.gov

Devices based on spectroscopy of atomic vapors can measure physical quantities such as magnetic fields, RF electric fields, time and length, and rotation and have applications in a broad range of fields including communications, medicine, and navigation. We present a type of photonic device that interfaces single-mode silicon nitride optical waveguides with warm atomic vapors, enabling precision spectroscopy in an extremely compact (<1 cm³) package. We perform precision spectroscopy of rubidium confined in a micro-machined, 27 mm³ volume, vapor cell using a collimated free-space 120 μm diameter laser beam derived directly from a single-mode silicon nitride waveguide. With this optical-fiber integrated photonic spectrometer, we demonstrate an optical frequency reference at 780 nm with a stability of 10⁻¹¹ from 1 to 10⁴ s. This device harnesses the benefits of both photonic integration and precision spectroscopy for the next generation of quantum sensors and devices based on atomic vapors.   © 2018 Optical Society of America under the terms of the OSA Open Access Publishing Agreement

OCIS codes: (300.6210) Spectroscopy, atomic; (120.3940) Metrology; (140.3425) Laser stabilization; (230.1950) Diffraction gratings; (230.3120) Integrated optics devices.

https://doi.org/10.1364/OPTICA.5.000443

1. INTRODUCTION

Precision spectroscopy of atomic vapors has long served as an enabling technology for quantum sensors [1,2]. It gains its utility through the combination of the sensitivity of atomic levels to external fields or perturbations and the use of light fields to control and interrogate the quantum state of the atom. Devices based on spectroscopy of atomic vapors can measure physical quantities such as magnetic fields [3], RF electric fields [4], time [5], length, and rotation [6], and have applications in the fields of communications, medicine, and navigation. While devices based on atomic vapors have reached the level of commercial deployment, they still typically rely on bulk optics and manual assembly. The integration of atomic vapors with photonic structures would provide an important building block for quantum devices and sensors. Photonic integration provides a path toward mass fabrication, but, more importantly, the use of photonic structures also provides the ability to tailor the properties of the light field to achieve a desired light–matter interaction.

Photonic structures used to probe warm atomic vapors typically fall into one of two geometries: either (1) a small waveguide where evanescent light interacts with atoms surrounding the waveguide or (2) a hollow core waveguide filled with atoms

[7]. The small waveguide geometry has been realized in both atomic cladding silicon nitride waveguides [8,9] and tapered optical fibers [10,11]. In these geometries, the light is confined to length scales of less than 1 μm. This tight confinement of the light can lead to strong atom–light interactions, enhancing nonlinear processes such as two-photon excitation or all optical switching. Recently, low-resolution Doppler broadened spectroscopy of methane using silicon photonic waveguides has been demonstrated for molecular gas sensing applications [12]. However, the small spatial overlap of the optical mode and atomic or molecular vapor make this method poorly suited for precision spectroscopy due to transit time broadening and intensity shift mechanisms. The hollow core waveguide geometry has been realized with ARROW waveguides [13] and hollow core photonic fibers [14–17]. The hollow core geometry allows for larger interaction volumes, with mode diameters as large as 85 μm in the case of the hollow core photonic crystal fiber, making it better suited for precision spectroscopy, as systematic effects such as light shifts and time of flight broadening are reduced [18,19]. However, the multi-mode nature of the guided fiber modes can lead to frequency shifts due to changes in mode-field overlap caused by coupling misalignment [19]. Here, we develop a third type

of geometry, where light is guided to the atoms using a single-mode Si_3N_4 waveguide, and then the light mode is expanded and coupled to free space using an extreme mode-converting apodized grating structure. In contrast with apodized grating structures typically used for coupling to optical fibers [20,21], in which the optical mode is expanded to a diameter of less than 10 µm, the mode converter described here expands the optical mode diameter from 500 nm in the waveguide to 120 µm in free space, corresponding to a mode area increase by a factor of more than 50,000. This allows us to take advantage of the integration and stability provided by single-mode Si_3N_4 photonics while enjoying the benefits of performing precision spectroscopy with a large free-space beam.

Here we demonstrate an optical frequency reference at 780 nm based on our photonic extreme mode converter and integrated micro-machined atomic vapor cell. The device achieves a precision of 10^{-11} at 100 s, while the photonic mode converter chip and vapor cell occupy a volume of less than 1 cm³. Other compact optical frequency references achieve a precision in the range of 10^{-13} to 10^{-11} at 100 s and rely on bulk optics and glass-blown vapor cells with volumes on the order of 100 cm³ [22–24]. The Si_3N_4 photonic platform provides for significant improvements in integration and volume, and the large transparency window of stoichiometric Si_3N_4, from 350 nm to >6000 nm, allows it to be used for a wide range of atomic and molecular vapors.

Direct integration with other Si_3N_4 photonic devices, such as microresonator frequency combs [25], could allow for compact broadband spectrometers.

2. EXPERIMENT SETUP

A. Photonic Chip Device

The overall layout of the photonic device is shown in Fig. 1. The device measures 9 mm × 14 mm and consists of Si_3N_4 waveguides on a silicon substrate that run from the edge of the chip and terminate in four pairs of extreme mode converters near the center of the photonic chip. Patterning of multiple gratings onto a single chip allows for testing of a range of design parameters using a single device. For work presented in this paper, a single grating is used. The waveguides have cross-sectional dimensions of 300 nm wide by 250 nm high and are fully etched and clad in silicon dioxide layers of ~2.9 µm thickness, as shown in Fig. 1(a). These waveguide dimensions support a single spatial mode for each polarization (TE and TM) of light at 780 nm. The guided light mode has a $1/e^2$ intensity diameter of approximately 500 nm. Light is coupled into the waveguides on the device via direct butt coupling from a single-mode fiber array, as shown in Fig. 1(b). The waveguides have an inverse taper at the edge of the chip to expand the guided mode diameter to better match the ~5 µm mode-field diameter of the single-mode fiber. After the
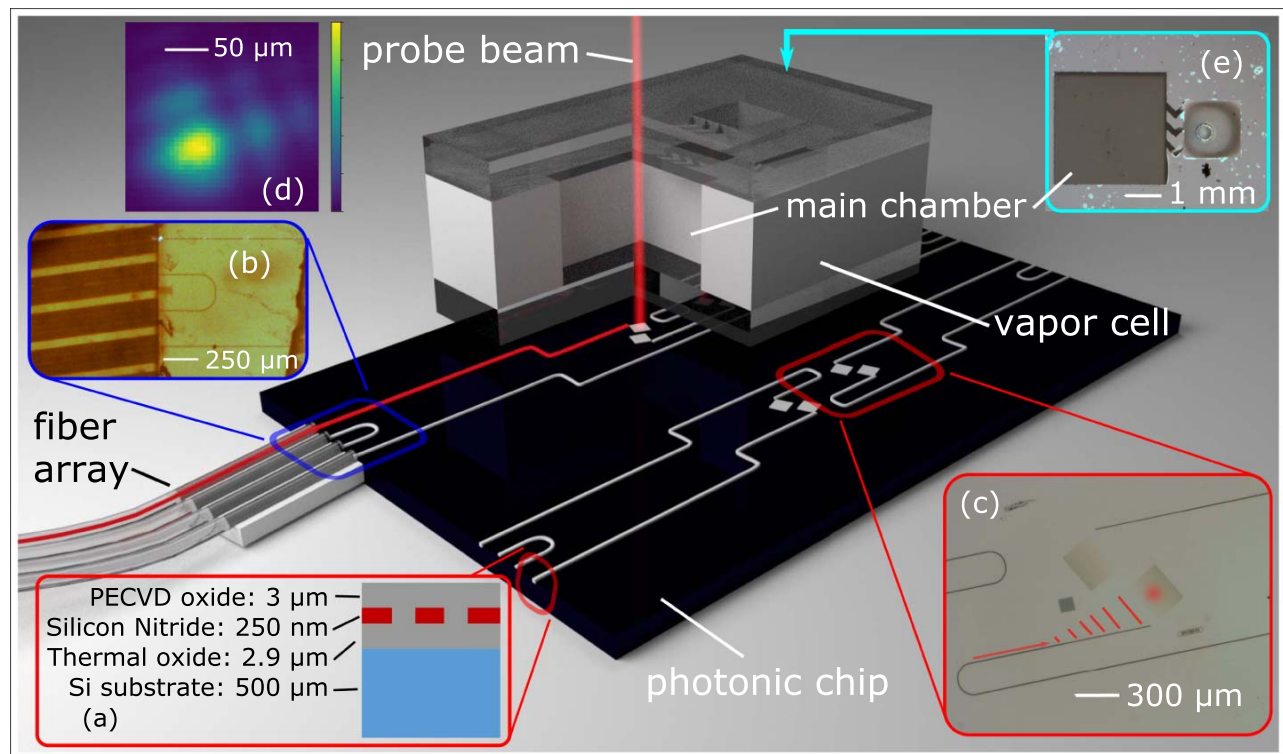

Fig. 1. Illustration of the photonic chip and micro-machined vapor cell. The photonic chip measures 9 mm × 14 mm and uses fully etched silicon nitride waveguides (shown gray) clad in silicon dioxide (not shown) to guide the light from the edge of the chip to the atomic vapor. For work described here, a single waveguide (shown red) and grating are used. (a) Layer structure of the photonic chip. (b) Microscope image of the four-port angled fiber array coupling light into the Si_3N_4 waveguide. The upper port couples light into the waveguide for spectroscopy. The middle two ports are connected via a ⊃-shaped loopback waveguide used for initial alignment of the fiber array. The bottom port is unused here. (c) Microscope image of the apodized grating extreme mode converters with the superimposed red marks indicating the evolution of the optical field before it is out-coupled into free space by the grating. (d) Profile of the laser beam out-coupled from the extreme mode converter imaged at a height of 8 mm above the surface of the chip. (e) Top-view microscope image of the micro-machined vapor cell after activation of the Rb dispenser pill. The large chamber to the left remains clear for optical access, while by-products from the Rb dispenser pill activation obscure the window to the small chamber on the right, which contains the dispenser pill.

fiber array is aligned to the photonic chip, the two are fixed to-gether with a UV-curing optical epoxy. By measuring the total transmission through the loopback waveguide [⊃ -shaped wave-guide Fig. 1(b)] using the middle two fiber array ports, we infer coupling efficiencies as high as −3 dB per facet. To expand the beam in the Si_3N_4 waveguide to a diameter of 100 μm and couple it to free space, we use a two-step process shown in Fig. 1(c). First, the beam is expanded in the direction transverse to propagation in the waveguide by evanescently coupling the light to the Si_3N_4 slab adjacent to the single-mode waveguide. The evanescent cou-pling is varied along the waveguide length to create a collimated Gaussian slab mode. The light propagating in the slab then im-pinges on an apodized grating structure that diffracts the light to above the surface of the chip at an angle of about 3° away from normal. The periodicity and duty cycle of the grating are designed to generate a near Gaussian beam profile with $1/e^2$ diameter of about 100 μm. Figure 1(d) shows an image of the diffracted beam recorded using a commercial CMOS camera taken at a height of approximately 8 mm above the photonic chip. About 50% of the total diffracted power is located in the main beam, which is well collimated with a divergence of 4 mrad and $1/e^2$ diameter of 120 μm at the surface of the chip. More information about the design and fabrication of the apodized grating extreme mode converters will be provided in a future publication [26].

To interface a rubidium vapor with the beam generated from the extreme mode converter, we use a separately constructed micro-machined silicon frame vapor cell [27], shown as a cutaway in the Fig. 1 illustration. The 2 mm thick silicon frame consists of two chambers that share a common vacuum space and are con-nected by angled baffles. The large chamber measures 3 mm × 3 mm and is designed to have clear optical access. The smaller chamber measures 1.5 mm × 1.5 mm and contains an alkali metal dispenser pill, consisting of rubidium molybdate and a zir-conium–aluminum reducing agent. To fabricate a sealed Rb cell, a borosilicate window is first anodically bonded to the bottom of the silicon frame to form a preform. The alkali dispenser is then placed in the preform, and the top window is anodically bonded to the preform under a vacuum of less than 10^{-6} Torr. To activate the Rb dispenser, a several-watt laser at 980 nm is focused onto the dispenser for a time of 1–10 s to optically heat the dispenser to a temperature greater than 450°C [28]. Figure 1(e) shows the cell after activation of the dispenser pill. The Rb stays condensed in the antechamber, and the angled baffles prevent solid by-products from the dispenser activation from contaminating the main chamber, allowing for good optical access. We have found that after multiple thermal cyclings of the cell from room temperature to 80°C, the Rb does migrate and form droplets at the cold spots at the center main chamber window. Nevertheless, the edges of the main chamber still provide enough optical access to transmit the beam from the grating expander clear through the micro-machined Rb vapor cell. Additional information about the micro-machined cell can be found in Supplement 1. The com-pleted cell is placed on top of the photonic chip without bonding for the work describe here.

To analyze the residual background gas in the Rb vapor cell generated during bonding and pill activation, we perform two-photon spectroscopy of Rb at 778 nm using a separate table-top setup [29]. This transition has the advantage of having a narrow natural linewidth of 667 kHz, making it a sensitive probe of other broadening mechanisms. With the cell shown in Fig. 1(e),

we observe two-photon linewidths of approximately 4 MHz. Assuming a typical broadening rate [29] of 50 MHz/Torr, this yields an estimate of background gas contamination in the MEMS cell of approximately 65 mTorr. Of this 65 mTorr, we expect about 3 mTorr to be from atmospheric helium that has diffused through the borosilicate windows, and the remainder to be from gases generated during cell bonding and Rb pill acti-vation (H_2, CO, etc.) [30]. The 65 mTorr corresponds to a pres-sure-broadening <1.3 MHz for the D2 transition in rubidium [31,32], smaller than the natural linewidth of 6 MHz.

B. Laser Stabilization

An overview of the laser stabilization setup is shown in Fig. 2. The system is based on a distributed Bragg reflector (DBR) laser at either 795 nm or 780 nm probing the D1 or D2 transition in an atomic rubidium vapor. The DBR laser, optical isolator, and variable optical attenuator are set up on a standard optical breadboard setup measuring 22.9 cm × 30.5 cm for convenience. The laser light is coupled into single-mode polarization maintain-ing fiber that terminates in a silicon V-groove fiber array for cou-pling directly to the edge of the photonic chip. As described in the previous section, the light propagates along the Si_3N_4 waveguide to the apodized grating extreme mode converter, where it then is collimated and directed up through the micro-machined rubid-ium vapor cell. A reflective neutral density filter with fractional transmission of 0.4 is placed above the vapor cell. The reflected portion of the beam is aligned to counter-propagate along the probe beam to provide the pump beam for a basic saturated
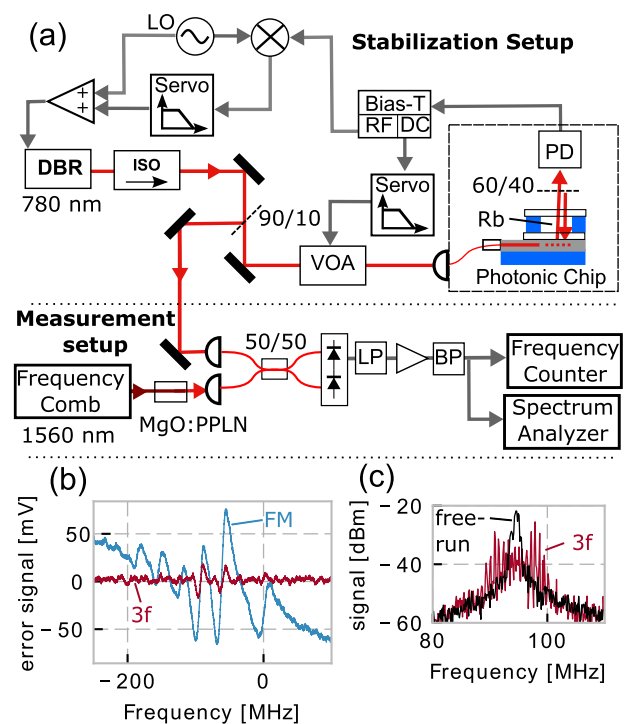

Fig. 2. Optical setup for laser stabilization. (a) Optical beams are shown in colored arrows. Electrical connections are shown in gray arrows. DBR, distributed Bragg reflector laser; ISO, optical isolator; VOA, var-iable optical attenuator; PD, photodiode; LO, local oscillator; LP, low pass filter; BP, band pass filter. (b) Error signals used for laser stabilization derived using FM and $3f$ spectroscopy. (c) Laser-OFC beat note for a free running and frequency dithered (3f) laser.

absorption spectrometer. We introduce a small misalignment of the retro-reflected beam to avoid additional etalons. The transmitted portion of the beam is detected on a fast photoreceiver. The resulting photoreceiver signal is used for laser intensity and frequency servo control. We chose this saturated absorption setup for its compact planar geometry and its simple implementation with a single optic. In principle, the partial reflector could be incorporated as an optical coating on the top window of the vapor cell, yielding a simple and extremely compact saturated absorption spectrometer. This simple setup leads to the situation where the probe beam is higher intensity than the pump beam, opposite of typical saturated absorption setups. This results in larger power broadening and light shifts than compared to more traditional saturated absorption setups that use either separate beams or additional polarizing optics to tune the relative intensities of the pump and probe beams [23,33]. Nevertheless, with this highly unoptimized compact geometry, we still achieve short-term frequency stability performance that is only a factor of 3 to 10 worse than the traditional table-top setups [23,33].

The fiber array and photonic chip are placed inside a temperature controlled box. The baseplate of the box is stabilized a few degrees Celsius above room temperature to maintain a constant temperature for the fiber array. The photonic chip is mounted on a separate temperature stabilized hot plate to maintain a temperature near 80°C. The elevated temperature sets the vapor pressure of Rb in the cell to achieve optimal signal to noise for the spectroscopy signal.

We investigate the performance of two laser stabilization techniques: frequency modulation (FM) spectroscopy and third-harmonic ($3f$) detection. To generate the error signal for locking the laser frequency, the DBR frequency is dithered via modulation of the injection current. For the FM spectroscopy setup, frequency sidebands are added to the laser via current modulation at a frequency of 15 MHz. A frequency mixer and low pass filter are used to generate the error signal shown in Fig. 2(b), corresponding to transitions from the ^{85}Rb ground hyperfine level $F_g = 3$ to excited $F_e = 2, 3, 4$ manifold. The error signal generated using FM spectroscopy has large, sharp dispersive peaks corresponding to the sub-Doppler hyperfine and crossover transitions. However, they are superimposed on top of a more slowly varying dispersive signal from the unsubtracted Doppler background. This baseline offset leads to an ambiguity in locking to the center of sub-Doppler peaks, which is undesirable for the intended use as a wavelength reference. For this reason, we also investigate third-harmonic detection, where the absorption signal is demodulated at three times the modulation frequency. The $3f$ error signal is largely free from Doppler background, though the overall signal amplitude is smaller. The third-harmonic error signal shown in Fig. 2(b) is shown for typical locking conditions, with a dither frequency of 100 kHz and excursion of 5 MHz. The probe beam contains 20 µW of power, which leads to a power-broadening of the spectroscopic lines to a width of ~30 MHz. The FM and third-harmonic error signals are both shown with a scan time of 150 ms and 300 Hz low pass filter bandwidth.

To monitor the performance of the frequency stabilized DBR laser, a portion of the laser beam is sent for heterodyne detection with an erbium fiber optical frequency comb (OFC). The repetition rate and offset frequency of the OFC are stabilized to a hydrogen maser enabling a fractional stability for the OFC of better than $1 \times 10^{-12}/\tau^{1/2}$ from 30 to 10^4 s, where τ is the averaging

period. The OFC generates light in the region of 1500–1600 nm. A portion of this light is frequency doubled to either 780 nm or 795 nm using a MgO doped periodically poled lithium niobate (MgO:PPLN) crystal. The DBR laser is combined with the doubled light from the OFC on a 50/50 fused fiber beam splitter and detected on a balanced photodiode pair. Figure 2(c) shows the laser-OFC beat note signal detected using an RF spectrum analyzer. The narrow peak shows the beat note of the free running DBR laser with no frequency modulation. The broad peak shows the beat note of the stabilized DBR laser when modulated at 100 kHz for $3f$ locking. When analyzing the signal from FM locking, the ± 15 MHz sidebands are filtered out using a narrow RF bandpass filter to ensure accurate frequency counting measurements. When locking using the $3f$ modulation technique, the signal-to-noise ratio of the beat note between the DBR laser and doubled OFC is too small to allow for reliable measurements using the frequency counter. Instead, we beat the DBR laser against an external cavity diode laser that has been stabilized to the same transition in Rb using a table-top saturated absorption FM spectroscopy setup similar to the one described in Ref. [33]. The frequency stability of the table-top setup has been independently measured using the OFC and is $3 \times 10^{-12}/\tau^{1/2}$ from 1 to 1000 s. This is sufficiently stable to characterize the photonic-based saturated absorption setup.

3. RESULTS

Figure 3 shows the typical performance of the DBR laser stabilized using the photonic chip and micro-machined vapor cell. Figure 3(a) shows a time trace comparing the frequency stability of the free running laser and the laser stabilized using FM spectroscopy. Unlocked, the DBR experiences fluctuations on the order of ~1 MHz at time scales longer than 1 s. When the laser is stabilized using the photonic chip and micro-machined vapor cell, the laser fluctuations are reduced to less than 10 kHz at times longer than 1 s. Figure 3(b) shows the non-overlapping Allan deviation for three different locking configurations. The performance for the three configurations is qualitatively similar. Each method shows a locking bandwidth on the order of several kilohertz, after which the frequency noise averages down as $1/\tau^{1/2}$ until it hits a flicker noise floor of 10^{-11} at $\tau \sim 100$ s. We estimate that the short-term performance of the device is limited by a combination of photon shot noise and detector noise, as they both contribute at a level of several $10^{-12}/\tau^{1/2}$, consistent with an overall device performance of $10^{-11}/\tau^{1/2}$.

For an initial examination of the long-term frequency stability of the photonic stabilization setup, we performed several systematic measurements using the 3f locking setup and stabilization to the ^{85}Rb, $F = 3 \rightarrow 2, 4$ crossover transition. We measured the laser power light shift to be –60 kHz/µW for the $1/e^2$ beam diameter of 120 µm, consistent with what has been measured before for similar transitions [33]. We typically probe the atoms with about 10 µW of laser power, corresponding to a frequency offset of about –600 kHz from the actual line center. The laser intensity servo is able to stabilize the laser intensity noise to better than 10^{-3} fractional stability at 1 s measured in-loop, corresponding to a frequency instability of 10^{-12}, well below that observed experimentally.

The frequency lock point is also sensitive to changes in cell temperature. The cell temperature can cause shifts in the lock frequency through several mechanisms. To observe these shifts we
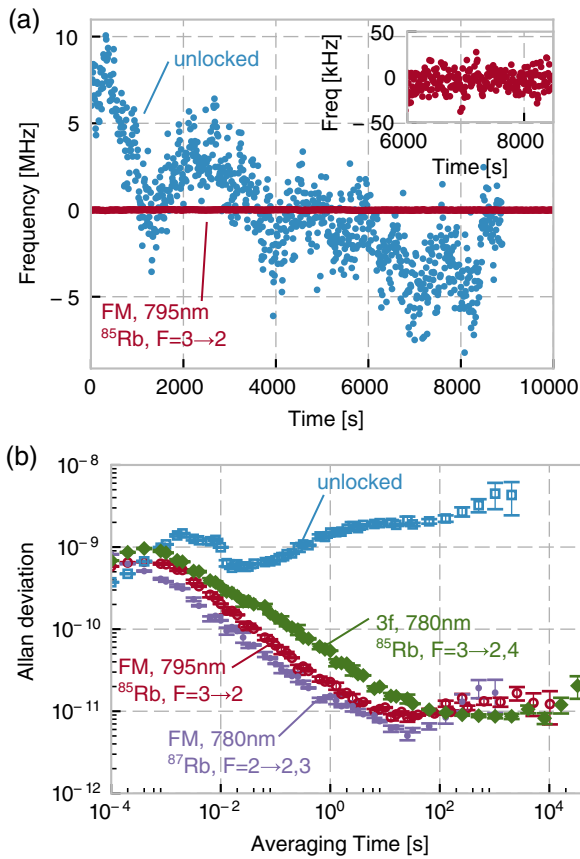
Fig. 3. Frequency stability of the DBR laser stabilized using the photonic spectrometer. For each measurement, the legends indicate the locking scheme (FM or $3f$) and the sub-Doppler transition used, where the notation corresponds to the hyperfine levels of $F_g \rightarrow F_e$. (a) Frequency counter measurements with a 10 s measurement time per point. The inset shows the locked signal on a finer frequency scale. (b) Allan deviation for the stabilized DBR laser.

Fig. 4. Photonic chip frequency sensitivity to temperature changes. (a) Transmitted laser power as the chip baseplate temperature is scanned by 7°C over an interval of 80 s. (b) Comparison of the observed frequency shift to that predicted by the change in measured laser power shown in panel (a) and the measured frequency shift of 60 kHz/μW.

scan the cell baseplate temperature from 76°C to 83°C over a period of about 90 s. During this time, the DBR laser remains locked to the cell and the rubidium density increases, as can be observed by the decrease in laser transmission shown in Fig. 4(a). The feedback to keep the laser intensity constant is not enabled during this measurement. The cell temperature effectively controls the density of Rb atoms in the vapor phase as a function of the saturated vapor pressure. We estimate the frequency shift due to the Rb–Rb collision shift for the observed temperature change to be negligible at less than 10 kHz [34,35]. More importantly, the Rb density also affects the average laser intensity over the interaction path length, due to the absorption of the probe beam by the Rb atoms. Thus, the Rb density temperature dependence couples the change in cell temperature to a change in light shift for fixed input laser power. For either of these mechanisms, a monotonic change in temperature would lead to a monotonic change in the stabilized DBR frequency. Figure 4(b) compares the observed frequency shift of the DBR laser with the shift predicted due to the observed change in average laser power. As the temperature is scanned, we observe large oscillations with an amplitude on the order of 100 kHz in the laser frequency, inconsistent with the small 50 kHz slow drift predicted by the 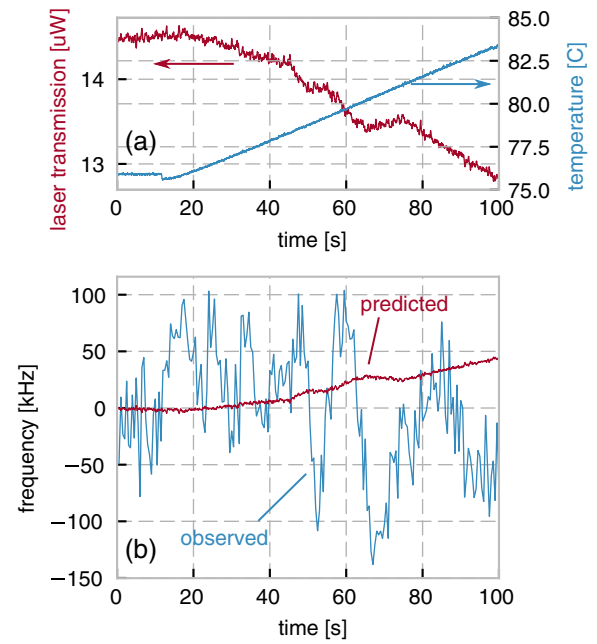change in average laser power. This oscillation is characteristic of the probe beam passing through an etalon whose length is changing as the cell temperature changes. In earlier versions of the experiment, we directly observed oscillations of the laser frequency due to an etalon that formed between a reflection at the fiber-to-waveguide interface and a reflection at the splice in the fiber array connector assembly. In this earlier setup, the V-groove array used flat ended fibers, allowing for a backreflection of several percent of the light at the fiber-to-waveguide interface. These etalons caused frequency oscillations with amplitudes of about ~1 MHz. Changing the fiber array to an 8° angle suppressed the backreflections by at least a factor of 100. We suspect the observed etalons may be due to backreflections inherent in the photonic grating mode converter itself, and we plan to investigate them in future chip designs.

Use of the OFC as a reference allows us to directly calculate the optical frequency of the stabilized laser and compare it to accepted values for the line center positions. For the FM locking, we do not expect close agreement due to the large shifts caused by the Doppler broadened background offset. Thus, we only compare here for stabilization using the $3f$ method for locking to the ^{85}Rb, $F = 3 \rightarrow 2, 4$ transition. Using the OFC, we calculate a detuning from line center of –385 kHz [36]. From measurements of our known systematic detunings, we can estimate an expected detuning from line center. The light shift contributes an offset of –600(30)kHz. From our earlier estimate of background gas contamination, we estimate a pressure shift contribution of –250 kHz. We estimate shifts on the order of ~ + 100 kHz from the etalon and measure a 2 mV electronic offset corresponding to a frequency offset of about +300 kHz. To estimate the contribution of the etalon fringe to the total frequency shift, we scan the cell temperature around the operating temperature to observe a full fringe [Fig. 4(b)] and assume the center value of the fringe

corresponds to the frequency shift in the absence of the etalon. Combining these shifts, we estimate an expected offset from line center of about –450 kHz, in reasonable agreement with the observed value of –385 kHz. Thus, we are able to achieve a frequency accuracy on the order of several hundred kilohertz, or a fractional accuracy of about 10^{-9}. Reducing this further will require higher purity Rb cells and reduction of the uncontrolled shifts due to etalons in the photonic system.

4. CONCLUSIONS

In summary, we have demonstrated and characterized a photonic optical frequency reference by performing on-chip precision spectroscopy of an atomic vapor. The photonic chip uses extreme mode converters based on apodized grating structures to transform a single guided mode in a Si_3N_4 waveguide to a low divergence ~100 μm diameter free-space beam ideal for precision spectroscopy. The device achieves a fractional frequency stability of 10^{-11} from 1 to 10^4 s. The stability and accuracy of the photonic chip are currently limited by shifts due to thermal drifts of etalons generated from backreflections in the waveguide.

Future work on this photonic precision spectroscopy platform can move toward both improved frequency stability performance and further miniaturization and integration. Previous work in our group has demonstrated that the micro-machined rubidium vapor cells can support fractional frequency stabilities below 10^{-11} by using larger probe beams generated with free-space optics either at 780 nm with beam diameter of 3 mm [37], or utilizing a narrower optical transition such as the rubidium two-photon transition at 778 nm. Thus, we expect that future photonic chip designs that reduce the etalons generated by the backreflections in the waveguide will lead directly to improved frequency stability. Wafer level mass fabrication of both the micro-machined vapor cells and the photonic chips may lead to inexpensive devices based on precision spectroscopy of warm vapors. For further integration, using multiple grating mode converters on a single device will allow for more complex laser beam geometries. Beams from adjacent gratings can be designed to overlap and counter-propagate after reflection from the top window, providing separate pump and probe beams. Alternatively, the probe beam can be reflected from the top of the cell and coupled back into an adjacent grating mode converter to allow for on-chip detection. Finally, the use of heterogeneous photonic integration techniques may allow incorporation of active components such as lasers and modulators allowing for complete integration of the spectroscopy platform [38].

See Supplement 1 for supporting content.

REFERENCES

1. J. Kitching, S. Knappe, and E. A. Donley, "Atomic sensors–a review," IEEE Sens. J. **11**, 1749–1758 (2011).
2. C. L. Degen, F. Reinhard, and P. Cappellaro, "Quantum sensing," Rev. Mod. Phys. **89**, 035002 (2017).
3. D. Budker and M. V. Romalis, "Optical magnetometry," Nat. Phys. **3**, 227–234 (2007).
4. J. A. Sedlacek, A. Schwettmann, H. Kübler, R. Löw, T. Pfau, and J. P. Shaffer, "Microwave electrometry with Rydberg atoms in a vapour cell using bright atomic resonances," Nat. Phys. **8**, 819–824 (2012).
5. S. Knappe, V. Shah, P. D. Schwindt, L. Hollberg, J. Kitching, L. A. Liew, and J. Moreland, "A microfabricated atomic clock," Appl. Phys. Lett. **85**, 1460–1462 (2004).
6. J. Simpson, Jr., J. Fraser and I. Greenwood, "An optically pumped nuclear magnetic resonance gyroscope," IEEE Trans. Aerosp. **1**, 1107–1110 (1963).
7. H. Schmidt and A. Hawkins, "Atomic spectroscopy and quantum optics in hollow-core waveguides," Laser Photon. Rev. **4**, 720–737 (2010).
8. L. Stern, B. Desiatov, I. Goykhman, and U. Levy, "Nanoscale light-matter interactions in atomic cladding waveguides," Nat. Commun. **4**, 1548 (2013).
9. R. Ritter, N. Gruhler, W. Pernice, H. Kübler, T. Pfau, and R. Löw, "Atomic vapor spectroscopy in integrated photonic structures," Appl. Phys. Lett. **107**, 041101 (2015).
10. M. Takiguchi, Y. Yoshikawa, T. Yamamoto, K. Nakayama, and T. Kuga, "Saturated absorption spectroscopy of acetylene molecules with an optical nanofiber," Opt. Lett. **36**, 1254–1256 (2011).
11. S. M. Hendrickson, M. M. Lai, T. B. Pittman, and J. D. Franson, "Observation of two-photon absorption at low power levels using tapered optical fibers in rubidium vapor," Phys. Rev. Lett. **105**, 1–4 (2010).
12. L. Tombez, E. J. Zhang, J. S. Orcutt, S. Kamlapurkar, and W. M. J. Green, "Methane absorption spectroscopy on a silicon photonic chip," Optica **4**, 1322–1325 (2017).
13. W. Yang, D. B. Conkey, B. Wu, D. Yin, A. R. Hawkins, and H. Schmidt, "Atomic spectroscopy on a chip," Nat. Photonics **1**, 331–335 (2007).
14. K. Knabe, S. Wu, J. Lim, K. A. Tillman, P. S. Light, F. Couny, N. Wheeler, R. Thapa, A. M. Jones, J. W. Nicholson, B. R. Washburn, F. Benabid, and K. L. Corwin, "10 kHz accuracy of an optical frequency reference based on $^{12}C_2H_2$-filled large-core kagome photonic crystal fibers," Opt. Express **17**, 16017–16026 (2009).
15. A. D. Slepkov, A. R. Bhagwat, V. Venkataraman, P. Londero, and A. L. Gaeta, "Spectroscopy of Rb atoms in hollow-core fibers," Phys. Rev. A **81**, 053825 (2010).
16. A. Lurie, P. S. Light, J. Anstie, T. M. Stace, P. C. Abbott, F. Benabid, and A. N. Luiten, "Saturation spectroscopy of iodine in hollow-core optical fiber," Opt. Express **20**, 11906–11917 (2012).
17. M. Triches, M. Michieletto, J. Hald, J. K. Lyngsø, J. Lægsgaard, and O. Bang, "Optical frequency standard using acetylene-filled hollow-core photonic crystal fibers," Opt. Express **23**, 11227–11241 (2015).
18. C. Perrella, P. S. Light, T. M. Stace, F. Benabid, and A. N. Luiten, "High-resolution optical spectroscopy in a hollow-core photonic crystal fiber," Phys. Rev. A **85**, 1–5 (2012).
19. P. S. Light, J. D. Anstie, F. Benabid, and A. N. Luiten, "Hermetic optical-fiber iodine frequency standard," Opt. Lett. **40**, 2703–2706 (2015).
20. X. Chen, C. Li, C. K. Y. Fung, S. M. G. Lo, and H. K. Tsang, "Apodized waveguide grating couplers for efficient coupling to optical fibers," IEEE Photon. Technol. Lett. **22**, 1156–1158 (2010).
21. K. K. Mehta and R. J. Ram, "Precise and diffraction-limited waveguide-to-free-space focusing gratings," Sci. Rep. **7**, 2019 (2017).
22. C. Affolderbach and G. Mileti, "Tuneable, stabilised diode lasers for compact atomic frequency standards and precision wavelength references," Opt. Lasers Eng. **43**, 291–302 (2005).
23. W. Liang, V. S. Ilchenko, D. Eliyahu, E. Dale, A. A. Savchenkov, D. Seidel, A. B. Matsko, and L. Maleki, "Compact stabilized semiconductor laser for frequency metrology," Appl. Opt. **54**, 3353–3359 (2015).
24. T. Kobayashi, D. Akamatsu, K. Hosaka, H. Inaba, S. Okubo, T. Tanabe, M. Yasuda, A. Onae, and F.-L. Hong, "A compact iodine-laser operating at 531 nm with stability at the 10^{-12} level and using a coin-sized laser module," Opt. Express **23**, 20749–20759 (2015).
25. Q. Li, T. C. Briles, D. A. Westly, T. E. Drake, J. R. Stone, B. R. Ilic, S. A. Diddams, S. B. Papp, and K. Srinivasan, "Stably accessing octave-spanning microresonator frequency combs in the soliton regime," Optica **4**, 193–203 (2016).
26. S. Kim, D. A. Westly, B. J. Roxworthy, Q. Li, A. Yulaev, K. Srinivasan, and V. A. Aksyuk, "Photonic waveguide mode to free-space Gaussian beam extreme mode converter," arXiv: 1803.08124 (2018).

27. L. A. Liew, S. Knappe, J. Moreland, H. Robinson, L. Hollberg, and J. Kitching, "Microfabricated alkali atom vapor cells," Appl. Phys. Lett. **84**, 2694–2696 (2004).

28. A. Douahi, L. Nieradko, J. C. Beugnot, J. Dziuban, H. Maillote, S. Guerandel, M. Moraja, C. Gorecki, and V. Giordano, "Vapour microcell for chip scale atomic frequency standard," Electron. Lett. **43**, 33–34 (2007).

29. N. D. Zameroski, G. D. Hager, C. J. Erickson, and J. H. Burke, "Pressure broadening and frequency shift of the $5S_{1/2} \rightarrow 5D_{5/2}$ and $5S_{1/2} \rightarrow 7S_{1/2}$ two photon transitions in ^{85}Rb by the noble gases and N_2," J. Phys. B **47**, 225205 (2014).

30. P. della Porta, C. Emil, and S. Hellier, "Alkali metal generation and gas evolution from alkali metal dispensers," in Proceedings of the 9th IEEE Conference on Tube Techniques, Technical Report TR 18 (1968), p. 246.

31. M. D. Rotondaro and G. P. Perram, "Collisional broadening and shift of the rubidium $D1$ and $D2$ lines ($5^2S_{12} \rightarrow 5^2P_{12}$, 5^2P_{32}) by rare gases, H_2, D_2, N_2, CH_4 and CF_4," J. Quant. Spectrosc. Radiat. Transfer **57**, 497–507 (1997).

32. N. D. Zameroski, G. D. Hager, W. Rudolph, C. J. Erickson, and D. A. Hostutler, "Pressure broadening and collisional shift of the Rb D2 absorption line by CH_4, C_2H_6, C_3H_8, n-C_4H_{10}, and He," J. Quant. Spectrosc. Radiat. Transfer **112**, 59–67 (2011).

33. J. Ye, S. Swartz, P. Jungner, and J. L. Hall, "Hyperfine structure and absolute frequency of the ^{87}Rb $5P_{3/2}$ state," Opt. Lett. **21**, 1280–1282 (1996).

34. P. Wang, A. Gallagher, and J. Cooper, "Selective reflection by Rb," Phys. Rev. A **56**, 1598–1606 (1997).

35. V. Vuletić, V. A. Sautenkov, C. Zimmermann, and T. W. Hänsch, "Measurement of cesium resonance line self-broadening and shift with Doppler-free selective reflection spectroscopy," Opt. Commun. **99**, 185–190 (1993).

36. A. Banerjee, D. Das, and V. Natarajan, "Precise frequency measurements of atomic transitions by use of a Rb-stabilized resonator," Opt. Lett. **28**, 1579–1581 (2003).

37. W. Loh, M. T. Hummon, H. F. Leopardi, T. M. Fortier, F. Quinlan, J. Kitching, S. B. Papp, and S. A. Diddams, "Microresonator Brillouin laser stabilization using a microfabricated rubidium cell," Opt. Express **24**, 14513–14524 (2016).

38. T. Komljenovic, M. Davenport, J. Hulme, A. Y. Liu, C. T. Santis, A. Spott, S. Srinivasan, E. J. Stanton, C. Zhang, and J. E. Bowers, "Heterogeneous silicon photonic integrated circuits," J. Lightwave Technol. **34**, 20–35 (2016).